



HAL
open science

Microstructural evolution of periclase under irradiation by molecular dynamics simulations

Alain Chartier, Paul Fossati, Laurent van Brutzel, Orest Dorosh, Jacek Jagielski

► **To cite this version:**

Alain Chartier, Paul Fossati, Laurent van Brutzel, Orest Dorosh, Jacek Jagielski. Microstructural evolution of periclase under irradiation by molecular dynamics simulations. *Journal of Applied Physics*, 2023, 133, pp.215902. 10.1063/5.0144673 . cea-04603812

HAL Id: cea-04603812

<https://cea.hal.science/cea-04603812v1>


Submitted on 6 Jun 2024

HAL is a multi-disciplinary open access archive for the deposit and dissemination of scientific research documents, whether they are published or not. The documents may come from teaching and research institutions in France or abroad, or from public or private research centers.

L'archive ouverte pluridisciplinaire **HAL**, est destinée au dépôt et à la diffusion de documents scientifiques de niveau recherche, publiés ou non, émanant des établissements d'enseignement et de recherche français ou étrangers, des laboratoires publics ou privés.

RESEARCH ARTICLE | JUNE 01 2023

Microstructural evolution of periclase under irradiation by molecular dynamics simulations **FREE**

Alain Chartier ; Paul Fossati; Laurent Van Brutzel; ... et. al



Journal of Applied Physics 133, 215902 (2023)

<https://doi.org/10.1063/5.0144673>



CrossMark

Articles You May Be Interested In

Phase study of $Mg_{1-x}Zn_xTiO_3$ powders prepared by dissolved metals mixing method

AIP Conference Proceedings (November 2022)

A comparison study in determining diphenylamine (DPA) in gun propellants by using two different methods (Soxhlet extraction with dichloromethane (DCM) and ultrasonic extraction (USE) with methanol methods)

AIP Conference Proceedings (November 2022)

Positron Annihilation Energy and Lifetime Spectroscopy Studies for Radiation Defects in Stainless Steel

AIP Conference Proceedings (March 2009)

AIP Advances

Why Publish With Us?

-  **25 DAYS**
average time to 1st decision
-  **740+ DOWNLOADS**
average per article
-  **INCLUSIVE**
scope

[Learn More](#)

Microstructural evolution of periclase under irradiation by molecular dynamics simulations

Cite as: J. Appl. Phys. 133, 215902 (2023); doi: 10.1063/5.0144673

Submitted: 31 January 2023 · Accepted: 13 May 2023 ·

Published Online: 1 June 2023



Alain Chartier,^{1,a)} Paul Fossati,¹ Laurent Van Brutzel,¹ Orest Dorosh,² and Jacek Jagielski^{2,3}

AFFILIATIONS

¹Université Paris-Saclay, CEA, Service de recherche en Corrosion et Comportement des Matériaux, F-91191, Gif-Sur-Yvette, France

²National Center for Nuclear Research, 05-400 Swierk/Otwock, Poland

³Lukasiewicz Research Network—Institute of Microelectronics and Photonics, Al. Lotników 32/46, Warsaw, Poland

^{a)}Author to whom correspondence should be addressed: alain.chartier@cea.fr

ABSTRACT

The response of MgO periclase to irradiation is investigated by means of molecular dynamics simulations, mimicking irradiation by Frenkel pairs accumulation. Both the calculated lattice and volume swellings, which refer, respectively, to the lattice and total volume changes reproduce well the experimental measures. The two diverge at around 0.2 dpa, above which lattice and volume swellings follow separate trends. Below this value, dislocation loops nucleate from point defects clusters, built up by progressive aggregation of both magnesium and oxygen interstitials. Very small $\frac{1}{2}\langle 110 \rangle$ loops lying in $\{001\}$ planes and made of $(\text{MgO})_6$ interstitials could be characterized. They serve as seeds for the subsequent growth of dislocation loops in all three $\{110\}$, $\{001\}$, and $\{111\}$ planes, which then follows a sublinear law. The $\frac{1}{2}\langle 110 \rangle$ loops lying in the $\{011\}$ planes become dominant as loop diameters increase beyond 15 nm. Above 0.2 dpa, we observe (i) the relative decrease of lattice swelling mainly because the very dense dislocations loops recombine and stabilize into less dense dislocation forests and, concomitantly, (ii) the fast increase of volume swelling caused by the occurrence of significant voids of up to 32 vacancies.

Published under an exclusive license by AIP Publishing. <https://doi.org/10.1063/5.0144673>

I. INTRODUCTION

The high radiation resistance of periclase MgO has been known for a long time.¹ Irradiation produces point defects and small clusters, which progressively transform into loops and eventually dislocation forests as the dose increases. This multi-stage evolution and transformation of isolated defects to more complex structures is intimately related to stress building and release.^{2,3} Indeed, this quite common phenomenological picture has been established, thanks to numerous experimental observations and theoretical investigations,⁴ as is detailed in the following.

Many authors have reported the presence of vacancies in periclase at the early stages of irradiation. Oxygen vacancies with trapped electrons—called F^+ centers—or oxygen divacancies—called F_2 centers—were commonly seen under proton,⁵ neutron,^{6,7} or electron irradiations.⁸ Cation vacancies without trapped holes—called V^{2-} center—or with trapped holes— V^- and V centers—have also been reported under proton⁵ and neutron irradiation.⁹ Cation and oxygen vacancies may aggregate and can form cavities. Cuboidal cavities of up to 100 vacancies have been observed under

neutron irradiation^{10,11} at high temperatures (above 1700 K). Implantation of light or heavy ions also promotes the formation of these cubic nano-cavities.^{12–14}

Fewer studies reported the evidence of interstitial formation. Due to their high mobility,^{15–20} they readily recombine with vacancies.²¹ This makes the experimental observation of interstitials difficult. Only oxygen interstitials were observed after neutron irradiation,⁹ with a specific split-interstitial configuration.⁷ Nevertheless, the existence of interstitials was called to support the interpretation of experimental observations^{22–26} based on general considerations, such as being the counterpart of vacancies. Theoretical studies devoted to the early stages of irradiation provide complementary details. Calculations of threshold displacement energies^{27–29} and simulations of displacement cascades^{30,31} showed that both magnesium and oxygen may stabilize as interstitials, with sometimes complex configurations. Theoretical studies pointed that single interstitials may relax as complex clusters of interstitials like octopolar building block of $(\text{MgO})_4$ ³² or hexa-interstitials made of eight Mg or O interstitials and two vacancies.^{33–35}

At high enough irradiation doses, perfect edge dislocation loops with $\frac{1}{2}\langle 110 \rangle$ Burgers vectors appear whether the irradiating particles were electrons,^{22,23} ions,^{24,36–38} or even neutrons.³⁹ These perfect loops are stoichiometric and of interstitial character. They lie in $\{110\}$ planes^{22,37,40} and exhibit elongated shapes along $\langle 100 \rangle$ directions with the major to minor axis ratio of about ten to one.²² Experimental observations²² showed that their nucleation stage is completed very early during irradiation. However, this step is still not fully understood despite numerous studies.^{20–24,32–35} This is likely because of the inherent complexity and too numerous contributing factors such as temperature,²² the initial presence of dislocations,¹⁹ and surfaces.⁴¹ Soon after nucleation, the density of loops reaches a saturation threshold, with a growth mode envisioned to be anisotropic.⁴² Their diameter increases with irradiation time at low temperatures according to a sublinear law.^{22–24} Furthermore, these loops interact with each other and evolve to form a dislocation network structure.^{1,39}

Macroscopic swelling is a visible consequence of the presence of defects created by irradiation in periclase. It has been documented for different conditions, including neutron^{39,43,44} and ion^{1,18,45} irradiations. This volume swelling can reach up to 3% at very high doses (around 30 dpa).⁴³ Starting from un-irradiated samples, their volume increases continuously with dose. This increase is rapid in a first stage, until around 0.2 dpa,^{1,39,45} and then slows down at higher doses (see Fig. 1). However, this macroscopic expansion is not necessarily consistent with lattice parameter measurements from the XRD experiments.^{1,39,45} Indeed, while the lattice parameter follows closely the volume swelling up to the same dose of 0.2 dpa, it then decreases for higher doses.^{1,39,45} This

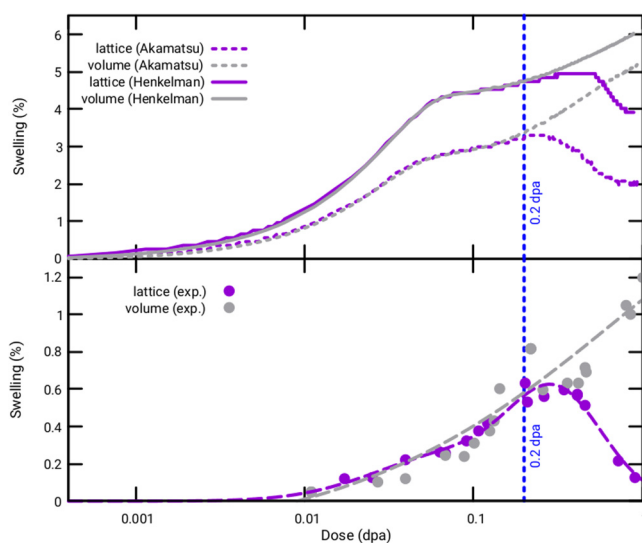


FIG. 1. Lattice swelling (purple lines and symbols) and volume swelling (gray lines and symbols) as a function of irradiation dose in dpa for MgO. The top panel shows the MD simulations with the Akamatsu and Henkelman potentials,^{46,47} and the bottom panel shows the experimental measurements.^{1,39,45} Dashed lines in the lower half are guides for the eyes.

change in behavior between the lattice parameter and macroscopic swelling has been explained as follows. Swelling at low doses (below 0.2 dpa) results from the presence of point defects.^{43,44} Their re-arrangements lead to the formation of dislocation loops and networks,^{1,39} which releases local strains and reduces the lattice parameter toward its equilibrium value. Re-arrangements become more likely as point defect concentration increases, which reduces their average separation distance and enables short-term combination mechanisms. As point defects recombine, the number and the size of voids continue their increase, causing the macroscopic volume swelling.

Overall, while the evolution of pristine periclase under irradiation is broadly understood, the atomistic details of the formation of dislocation loops from point defects and their links with macroscopic and lattice swelling remain unknown. In this article, we provide insights on these two points. For that purpose, we investigate the response to the irradiation of periclase MgO using molecular dynamics (MD) simulations with the Frenkel pairs accumulation (FPA) technique.^{48,49} Accurate analysis of these simulations provides insights on the mechanisms at the origin of the nucleation of dislocations and on the discrepancy between volume and lattice swellings.

II. TECHNICAL DETAILS

Numerous theoretical studies^{27–31} have been dedicated to primary damages produced by irradiation in MgO in the ballistic regime. Most of these studies employed MD simulations of displacement cascades, which provide valuable information on single ballistic events, which is the typical case in heavy ion irradiations at low energy, for example. The results of these simulations demonstrated that cascade events produce almost only small defects such as single vacancies, single interstitials, and small clusters of interstitials.^{27–31} Primary irradiation events (with the only exception of very high energy ions creating tracks via electronic energy losses) never induce direct impact amorphization, that is, the creation of a metastable amorphous volume. It is, therefore, attractive to bypass primary events, which are computationally costly as they require long simulations to equilibrate and to consider the remaining defects as a starting point of the simulations. This is the purpose of the Frenkel pairs accumulation (FPA) methodology,^{48,49} in which point defects are introduced over time. Indeed, this FPA methodology opens access to the dose effect, i.e., the accumulation of damages induced by irradiation, by enabling precise control of the number of displaced atoms. It also simultaneously circumvents the time-consuming overlap of cascades that would be necessary otherwise. Apart from this shortcut, it is worth mentioning that FPA does reproduce light particle irradiation, such as electron irradiation. This is because the methodology precisely consists in introducing point defects—in the form of Frenkel pairs—just like electron irradiation does.

In the present study, we use a modified version of the LAMMPS molecular dynamics simulator,⁵⁰ in which we have included the FPA methodology. We employ both Akamatsu⁴⁶ and Henkelman⁴⁷ empirical potentials for the description of MgO. Both of them are based on the Buckingham description of all interatomic interactions, in which partial charges are set fixed. This precludes

any description of defects implying charge transfer—like vacancies with trapped electrons, for example—reported in the experiments.^{5–9} Nevertheless, these potentials have been found to produce accurate results in investigations of several defect-related phenomena. For example, the Akamatsu potentials were used to explore self-diffusion in periclase (MgO) in a broad range of temperature and pressure conditions,⁵¹ whereas the Henkelman potentials were extensively used in studies related to irradiation damages^{33,35} or mechanical properties,^{52–54} with a particular focus on dislocations. With these extended and different domains of applications, we expect to extract general features when investigating MgO exposed to irradiation and to exclude any bias that could be attributed to empirical potentials.

We perform our calculations with supercells of 7 077 888 atoms, which corresponds to a volume slightly bigger than $40 \times 40 \times 40 \text{ nm}^3$. During the FPA process, 3200 magnesium and oxygen Frenkel pairs (FPs) are created at the same time at regular intervals. The choice of double introduction differs from previous studies on oxides in which cation FPs only were created.^{55–57} This choice was well founded, for example, in oxides with the fluorite structure, which exhibit two distinct regimes for cations and oxygen, with quite different threshold displacement energies^{58,59} and diffusion coefficients.⁶⁰ In contrast, periclase shows similar behaviors for both magnesium and oxygen ions.^{29,51,61} In particular, threshold displacement energies for magnesium and oxygen are close to each other, 88 and 92 eV, respectively.²⁹ This means that similar amounts of defects of either chemical species remain after a single ballistic event.³³ Therefore, both elements cannot be uncoupled, and both of them need to be introduced simultaneously during FPA. Additionally, Aidhy *et al.*³² have shown previously that the introduction of only magnesium or oxygen FPs results in enhanced annealing, and subsequently, a complete healing of the damage. Regarding the time interval of FP creation, we set the value at 2 ps because it is known to be sufficient for most defects to re-arrange or recombine^{30,35} at short distances. This time interval is, nevertheless, too short to account for any thermal diffusion.

The introduction of FPs leads to an increase of the stress around each defect.⁵⁵ Part of this stress transforms into heat during re-arrangement or recombination. Both stress and heat excesses have to be handled during the simulations to prevent any unphysical behavior, such as artificial melting. For this purpose, we use a Berendsen barostat and a Berendsen thermostat in order to drive the system back to the target room pressure and temperature, within the time interval of FP introduction.

Since the FPA procedure creates both oxygen and magnesium FPs, it is quite natural to count the damage as displacement per atom (dpa). This measure sounds very similar to the one commonly used, but a direct comparison with the experimental counterpart is questionable.⁶² Nevertheless, the present results show that the calculated dose is comparable to estimates from experiments and, therefore, a reliable measure of the damage.

The dose rate simulated by FPA is very high (4.5×10^8 dpa/s) and obviously much higher than any experiments can reach, which is at best around 10^{-2} dpa/s. Again, this does not preclude a reliable simulation of the response of periclase to irradiation as already observed in many other oxides.^{48,49,55–57} This might also indicate

that part of the response to the irradiation of oxides relies on short time/short-range recombination of defects at least as much as longer-term diffusion, as will be shown below. It is, nevertheless, worth mentioning that because of the high dose rate employed, our FPA simulations best describe low temperature behavior, which is dominated by athermal recombination. In addition, at such very high rates, dose rate effects are limited, which prevents a full investigation of such effects.

We analyze the evolution of periclase as a function of the irradiation dose with different tools, using selected snapshots of our MD simulations. Atomistic analysis is carried out with a home-made code based on the topological representation of the crystal structure, well sensitive to isolated vacancies and interstitials, and more importantly to complex configurations of interstitial clusters and very small dislocation loops. From this analysis, we determine the size (diameter) and the habit plane of each loop by principal component analysis. The detection of dislocation lines is performed with the DXA algorithm implemented in OVITO.⁶³ In parallel, we record the evolution of volume and lattice swellings. The former is simply the volume of the supercell, which corresponds to macroscopic observations. For the lattice swelling, we calculate x-ray powder diffraction (XRD) pattern for each MD snapshot using the Debyer software⁶⁴ and we simply index the peaks.^{55,57} This measure quantifies the strains applied to the lattice.

III. MgO IRRADIATED BY FPA AT CONSTANT PRESSURE

First, we compare the evolution of the lattice and volume swellings calculated with both Akamatsu and Henkelman potentials with experimental measurements (see Fig. 1). We observe that both potentials predict similar swellings. For each potential, both lattice and volume swellings are equal up to 0.2 dpa. They separate at 0.2 dpa, where lattice swelling saturates. Above 0.2 dpa, volume swelling continues to increase, while lattice swelling peaks and then decreases.

Such behaviors are very similar to experiments, where the difference between lattice and volume swellings appears at the exact same dose of 0.2 dpa. This indicates that simulations capture the relevant mechanisms at both macroscopic and microscopic scales, as was already observed in fluorites.^{55–57} However, some differences between experiments and simulations deserve comments. We note that the swellings obtained in simulations are four times greater than those obtained in experiments. Such overestimation is known and documented in Urania, for example.⁵⁵ This is related to the very high density of defects introduced during FPA simulations. Because of the time scales considered, these defects cannot anneal in MD simulations. Furthermore, no stair step increase below 0.2 dpa is observed in the experiments. As will be explained below, these step-like shapes are related to the high density of loops, which significantly contribute to both lattice and volume swellings.

A. Microstructure transformation with irradiation dose

We report more details of the evolution of MgO as a function of dose in Fig. 2 for the Akamatsu potentials and Fig. 3 for Henkelman potentials. Both figures show the volume and lattice swellings as a function of dose along with the evolution of the

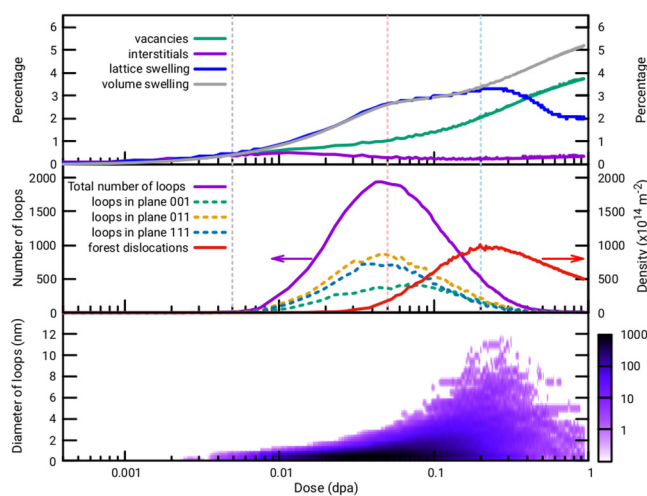


FIG. 2. Defects and swelling as a function of dose in irradiation simulations using the FPA method and the Akamatsu potentials;⁴⁶ the top panel shows the evolution of the lattice (blue line) and volume (gray line) swellings as a function of dose in dpa as well as the concentrations of vacancies (green line) and interstitials (purple) for both Mg and O; the middle panel provides details on the number of $\frac{1}{2}\langle 110 \rangle$ loops (total—purple line and different lying planes—dashed lines) and the density of forest dislocations (red line) of $\frac{1}{2}\langle 110 \rangle$ character for most of them; the bottom panel is the density map of the evolution of the diameter of loops with dose. The vertical dashed lines indicate the transition thresholds discussed in the text.

concentrations of point defects (top panels), the number and density of dislocations loops in different habit planes (middle panels), and the distribution of the diameters of dislocation loops as a function of dose (bottom panels).

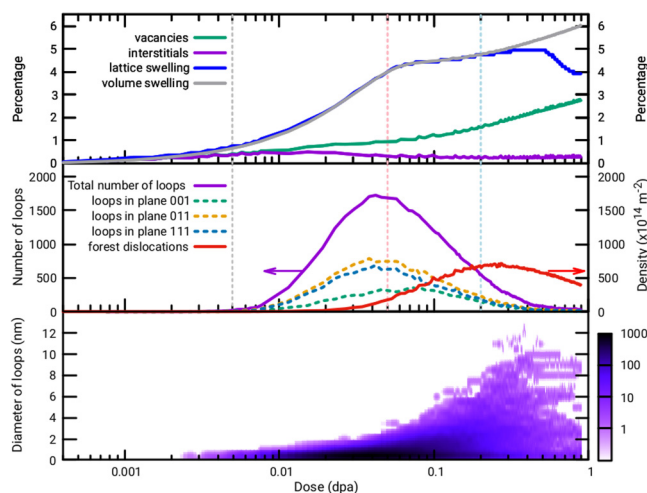


FIG. 3. The three graphs report the analysis of the simulations performed with the Henkelman potentials.⁴⁷ Symbols and lines are the same as in Fig. 2.

Before any detailed analysis, it is worth mentioning that the response of MgO to irradiation modeled by FPA is similar to both Akamatsu or Henkelman potentials^{46,47} for all measured parameters, not only swellings as already mentioned. The microstructure evolution shows successive stages, which have already been observed in other materials.^{55,57} In these figures, we can make out four different stages separated by dashed lines.

The first stage is characterized by the presence of the point defects created by FPA. Both interstitials and vacancies are present in identical amounts and increase with dose. This stage lasts up to around 5×10^{-3} dpa (vertical dashed line in gray in Figs. 2 and 3) where the behaviors of interstitials and vacancies differ (upper graphs). This threshold dose is the same for both potentials. In this low-dose regime, the point defects induce supercell swelling. Both lattice and volume swellings remain equal as they increase, reaching around 0.25% at 5×10^{-3} dpa.

The second stage starts at 5×10^{-3} dpa, when the concentration of interstitials and vacancies starts to differ. For doses above 5×10^{-3} dpa, the concentration of vacancies continues to increase as the concentration of interstitials saturates and starts to decrease. This decrease is concomitant with the stabilization of interstitial clusters, which nucleate during the FPA and will be described in another section. These clusters of interstitials transform into dislocation loops, which thrive at the expense of single interstitials (middle and bottom panels in Figs. 2 and 3). An illustration is given in Fig. 6(a) where some loops are highlighted in red. Most loops are perfect dislocations loops with $\frac{1}{2}\langle 110 \rangle$ Burgers vectors. They lie in $\{001\}$, $\{110\}$, and $\{111\}$ planes, with a smaller number of loops lying in the $\{001\}$ planes than in the two other planes. Loops are associated with large strains to MgO, which result in an increase in the slope of both lattice and volume swellings with dose. Lattice and volume swellings remain very close and reach around 2% at 5×10^{-2} dpa. This second threshold is identical for both potentials and corresponds to a pronounced decrease in the rate of growth of both swellings as well as a maximum in the total number of loops.

The third stage is marked by the decrease in the number of loops between 5×10^{-2} and 2×10^{-1} dpa. This decrease results from the interactions between dislocation loops, causing coalescence and transformation of the loops into a dislocation forest (see the loops highlighted in red in Fig. 6). At the same time, interstitials mostly disappear, while vacancy concentration continues its growth. Single magnesium and oxygen vacancies combine above 0.1 dpa and form cavities larger than two Schottky defects $[(\text{MgO})_2]$, see Figs. 4 and 5]. This combination can occur, thanks to the room left in by sparse dislocations. Some $(\text{MgO})_4$ Schottky clusters have cubic shapes similar to those reported experimentally under different irradiation conditions.^{11,12} Lattice and volume swellings jointly increment, at a moderate rate compared to stage II. This is related to two conflicting contributions. On one hand, the decrease in the number of loops releases some of the strains and, therefore, reduces swelling. On the other hand, the development of the dislocation forest tends to increase swelling. In that regime, the concentration of vacancies increases moderately, following the dislocation density of the forest. At 0.2 dpa, lattice and volume swellings begin following different trends. This change is concomitant with the maximum diameter reached by dislocation

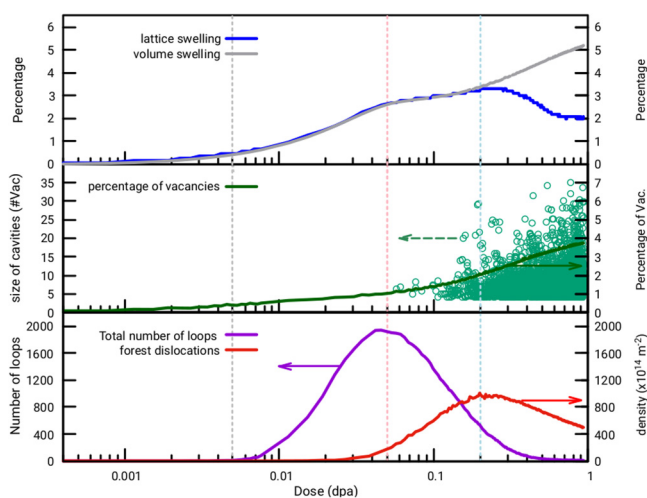


FIG. 4. Analysis of the simulations performed with the Akamatsu potentials:⁴⁶ the top panel shows the evolution of the lattice (blue line) and volume (gray line) swelling as a function of dose (dpa); the middle panel provides the total concentration of vacancies (green lines) and the size of cavities of more than $(\text{MgO})_2$ (green circles) as a function of dose; the bottom panel reports again the evolution of the number of $\frac{1}{2}\langle 110 \rangle$ loops (purple line) and the density of forest dislocations (red line) as a function of dose. Vertical dashed lines indicate the transitions discussed in the text.

loops (see the bottom panels of Figs. 2 and 3) and the highest density of the dislocation forest.

The fourth last stage, which starts at 0.2 dpa, is notable for the decrease in the number of dislocations and the disappearance of loops. Considering loops, they decrease not only in number but

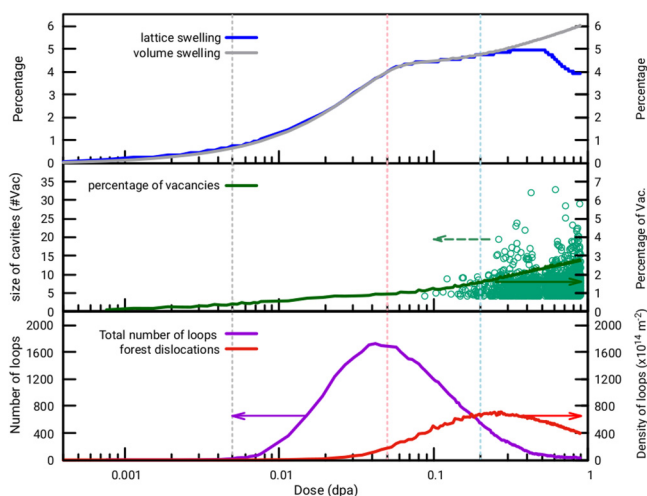


FIG. 5. The three graphs report the analysis of the simulations performed with the Henkelman potentials.⁴⁷ Symbols and lines are the same as in Fig. 4.

also in maximum size, reduced from around 10 nm at 0.2 dpa to 4 nm at 1 dpa. The structure stabilizes, leaving the dislocation forest and a few loops as shown in Fig. 6(b). This results in a release of the lattice stress from dislocations and, therefore, to the decrease of the lattice swelling. On the contrary, the amount of vacancies strongly increases with dose at this stage. A significant part of them contribute to the stabilization of cavities with sizes ranging from $(\text{MgO})_4$ to $(\text{MgO})_{16}$ (4–16 Schottky defects, see again Figs. 4 and 5). They can thrive thanks to the decrease of the amount of dislocations. The increasing presence of cavities also correlates with the rapid amplification of the volume swelling. Hence, volume swelling is unsurprisingly related to the number of vacancies⁶⁵ and, interestingly, their contribution to the swelling is amplified with their gathering as cavities.

B. Nucleation and growth of loops

In this section, we bring some additional details on the nucleation and growth of loops and, in particular, on the small clusters and the small loops during stage II described above. We do know already that interstitials—either magnesium or oxygen—gather together to form loops.^{30,33–35} This can be observed in our results with the correlation between the decrease in the number of interstitials and the apparition of dislocation loops (Figs. 2 and 3).

Previous findings made by Uberuaga *et al.*^{30,33–35} showed the first steps of interstitials clustering. Because of strong electrostatic interactions, magnesium and oxygen interstitials quickly combine to form MgO di-interstitials or anti-Schottky defects.^{33,35} These di-interstitials become less mobile compared to single interstitials. They capture isolated interstitials and grow as tri-interstitials, and then as tetra-interstitials formed of two clustered anti-Schottky defects. Tetra-interstitials are very stable,^{30,35} and they can continue growing by capturing interstitials in their vicinity.³⁵ They transform into bigger very mobile hexa-interstitial clusters^{33–35} and subsequently into octa-interstitial clusters.

Apart from the quick formation of MgO di-interstitials (anti-Schottky), which occurs within a few picoseconds, most re-organizations described above have characteristic times of the order of nanoseconds at least and up to seconds, which may appear hardly obtainable by direct molecular dynamics simulations. In our simulations, the high dose rate of Frenkel pairs of magnesium and oxygen biases the simulations, resulting in high concentrations of point defects and putting interstitials—indifferently of magnesium or of oxygen—within the reach of clusters. As a consequence, many interstitial clusters already seen in previous studies,^{30,32–35} including tri-interstitials or tetra-interstitials, are observed in the present simulations. We show in Fig. 7, for example, the specific one made of two anti-Schottky and one Mg close Frenkel pair. This cluster is known to be the seed of bigger ones according to Aidhy *et al.*³²

Larger interstitial clusters are found in qualitatively different structures, taking the form of interstitial $\{001\}$ planes rather than the cube-based structure of di- and tetra-interstitials, which are not associated with vacancies. Such a planar conformation of hexa-interstitial clusters $(\text{MgO})_3$ has been identified as a building block for the construction of larger octa-interstitial $(\text{MgO})_4$ clusters and even clusters up to $(\text{MgO})_8$.³³ These clusters become more

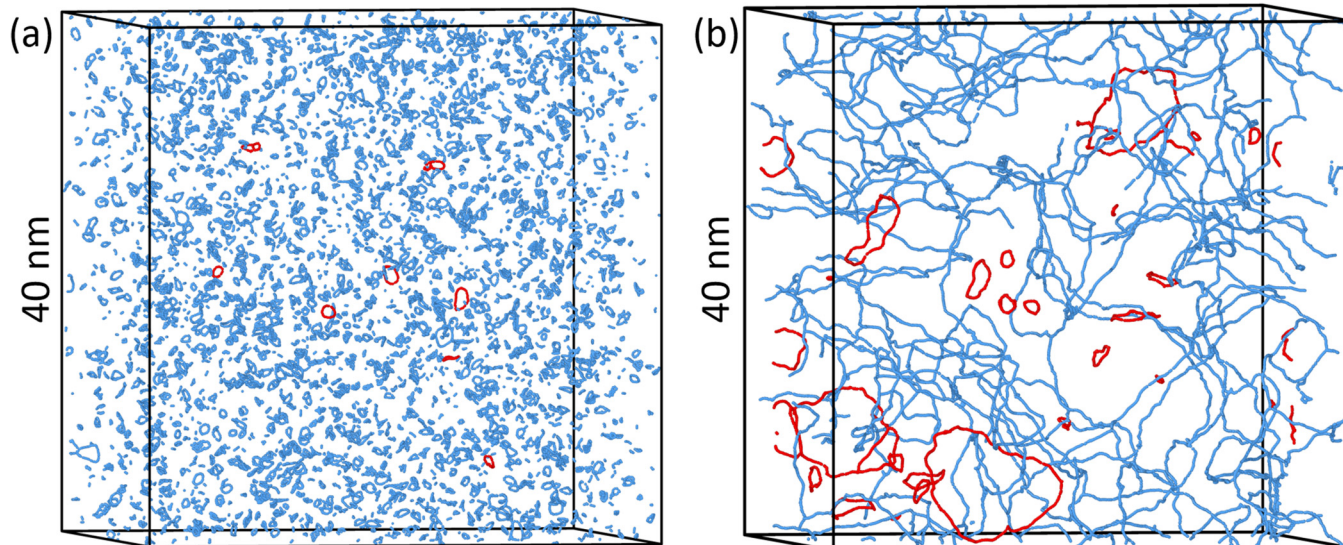


FIG. 6. Snapshots of MgO irradiated by Frenkel pairs accumulation at 0.015 dpa (a) and at 0.9 dpa (b) with Henkelman potentials.⁴⁷ Lines represent the $\frac{1}{2}\langle 110 \rangle$ loops and $\frac{1}{2}\langle 110 \rangle$ dislocation lines. Red lines highlight the examples of isolated loops of various sizes and orientations, with some coalescent loops at 0.015 dpa (a).

favorable as their sizes increase, providing a driving force for the coalescence of isolated interstitial or anti-Schottky defects into such larger clusters.

Figure 8 shows two examples of similar $\{001\}$ octa-interstitial defects, which, nevertheless, result in different defect structures. In the first one, the ions belonging to the supplementary plane are on interstitial sites of the rock salt structure [Figs. 8(a)–8(c)]. In this situation, the interstitial plane pushes apart the adjacent $\{001\}$ planes of the crystal. Most of the displacement being perpendicular to the plane of the defect. However, the additional plane can also be shifted, in such a way that at least some of its ions can be part of valid Mg–O–Mg lines involving the surrounding crystal lattice [Figs. 8(d)–8(f)]. The relaxation in this case involves some shear along the interstitial plane, with rows on one side of the interstitial

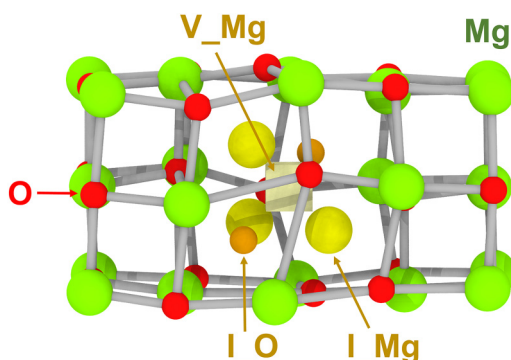


FIG. 7. Cuboid like tetra-interstitial defect made of two anti-Schottky and one Mg close Frenkel pair observed in the present simulations.

plane ending up aligned with a neighboring row on the other side. Considering a slice perpendicular to the defect plane, as in Fig. 8(f), a Burgers circuit can be set up with a Burgers vector of $\frac{1}{2}\langle 011 \rangle$, highlighting the dislocation character of this defect cluster.

During FPA simulations, the defects we observe are more complex than this simplified picture. While small clusters have the general structure of the tetra-interstitial cluster, i.e., the central vacancy and the interstitials arranged on the corners of a cube around it, they generally have additional interstitials, resulting in a small overall electric charge, usually of ± 2 . Similarly, the interstitial planes are rarely electrically neutral, and the exact arrangement of the atoms varies. A common structure is shown in Fig. 9, which is a dodeca-interstitial $(\text{MgO})_6$ cluster with an additional oxygen ion and, therefore, a negative effective charge. Due to the constant production of Frenkel pairs, the crystal has a population of vacancies and interstitials that can effectively compensate the clusters' charges.

Our observations are consistent with successive steps in the formation of dislocations under irradiation. Initially, interstitial clusters in cube-like structures, often around less mobile vacancies. As the clusters grow by the coalescence of mobile interstitials, they form interstitial planes, which distort the surrounding lattice and form dislocation loop nuclei. The exact point at which defect structures transform from cubic clusters to interstitial planes is unclear. However, our simulations show qualitatively that clusters larger than 10 interstitials are all dislocation loops. The smallest loops observed in FPA simulations are octa-interstitial clusters similar to that shown in Fig. 8, but these are very rare compared to larger loops such as deca-interstitials or dodeca-interstitials similar to what is shown in Fig. 9. This is reminiscent of a dislocation nucleation mechanism involving a similar transition between a three-dimensional defect structure and interstitial dislocation loops in iron.⁶⁶

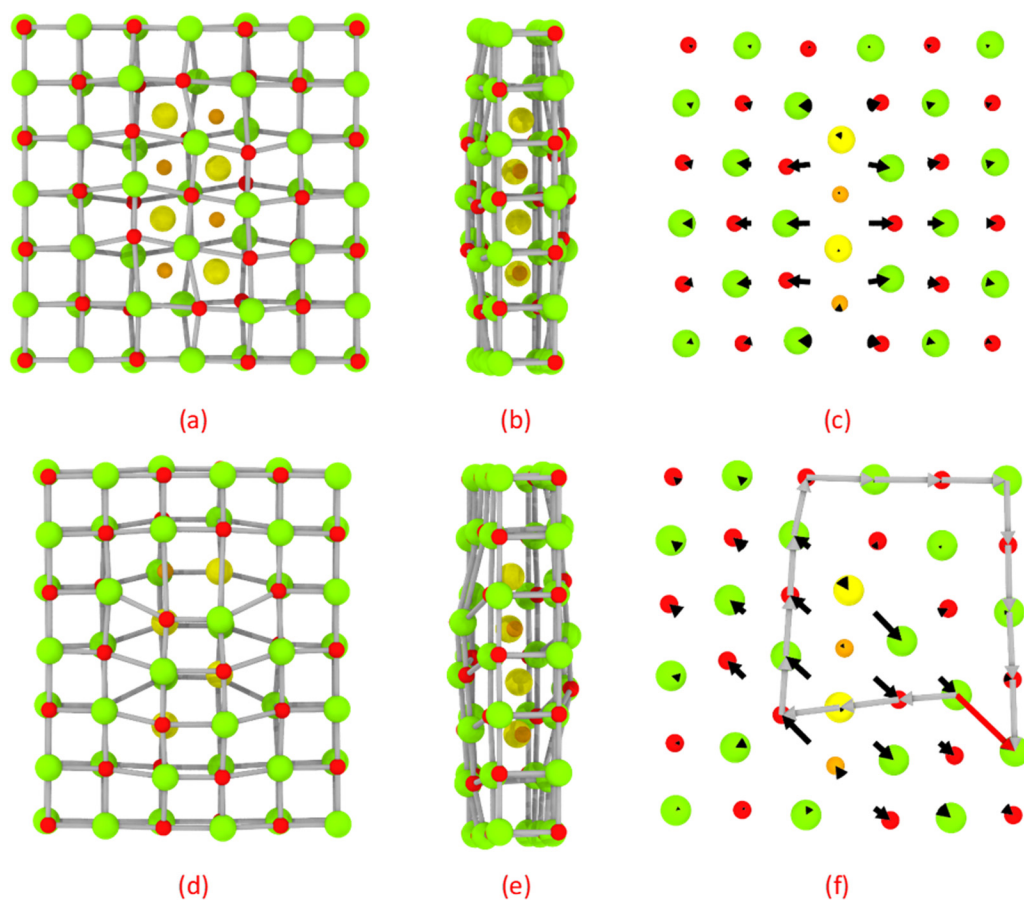


FIG. 8. Structure of octa-interstitial planes in MgO after relaxation using the Akamatsu potential. The top row shows the defect as an interstitial cluster: (a) front view; (b) side view; (c) map of atomic displacements relative to the perfect structure. The bottom row shows the same defect as an interstitial dislocation loop: (d) front view; (e) side view; (f) atomic displacement map, with a Burgers circuit indicated by the gray arrows and the resulting Burgers vector in red.

We turn now to the growth of dislocation loops that is determined by recording the diameter d (nm) of each loop regardless of its orientations. For analysis purposes, the diameter range is broken up into nine 0.5 nm-wide bins between 0.5 and 4.5 nm, and the number of loops falling in each bin is counted. The analysis is performed over the course of simulations using both Akamatsu and Henkelman potentials, resulting in the data shown in Figs. 10 and 11, respectively. We use a lognormal distribution to fit the relaxation times of each diameter window (full lines in bottom panels). The choice of a lognormal distribution is motivated by the consideration that the growth of loops is multi-parametric:⁶⁷ magnesium and oxygen interstitials located in the vicinity of the loop edges feed their growth while close vacancies deplete them. The global maximum (diameter d) of each distribution is then plotted as a function of dose (upper panels in Figs. 10 and 11). It marks the onset of the decrease of loops of a given diameter for the benefit of bigger ones.

We observe—as expected—that small loops disappear with dose (or equivalently with time) and smoothly transform into bigger ones. The growth follows a sublinear law (purple line upper

panels). The diameter (d) of loops evolves with time (t) like $d \propto t^{0.83}$ and $d \propto t^{0.70}$ for Akamatsu and Henkelman, respectively. These exponents are in agreement with the low temperature regime (below 900 K) reported experimentally.^{22–24} In this low temperature regime, only interstitials are mobile and are understood to serve as the stable nuclei of interstitial loops.^{22–24}

Note that the population of loops of each diameter decreases with dose. This is related to two parameters: the coalescence of small loops into bigger ones and their ultimate transformation into dislocation forests (see again the middle panels of Figs. 2 and 3).

C. Stability of dislocations

Experimental observations consistently show^{22,23} the nucleation of $\frac{1}{2}\langle 110 \rangle$ loops lying in the $\{110\}$ planes in MgO single crystals (cut along the 001 direction) irradiated by electrons and more largely in any irradiation conditions, being neutron irradiation or ion irradiations.^{24,36,37,39,40} These prismatic loops are of interstitial type, and they are elongated along the $\langle 010 \rangle$ directions.^{22,23} Their

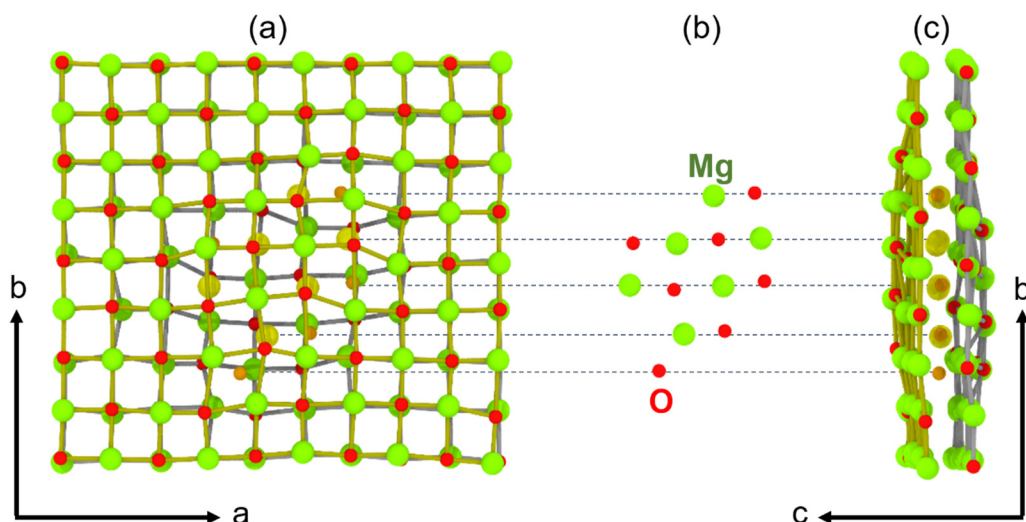


FIG. 9. Close-up views of small platelet or $\frac{1}{2}\langle 011 \rangle$ loop lying in the $\{001\}$ plane from the top (a) and (b) and from the side (c). View (b) shows the platelet isolated from the rest of the lattice. Shifts of $\frac{1}{2}\langle 011 \rangle$ between the lattice and the platelet can be seen on (a) and (c). Note the strain imposed by the platelet to the lattice along the c -axis on (c).

diameter ranges from 2 nm up to a few micrometers.^{22–24} In our simulations, neither $\frac{1}{2}\langle 110 \rangle\{001\}$ loops nor $\frac{1}{2}\langle 110 \rangle\{111\}$ loops are observed in any irradiated MgO regardless of the conditions. Calculations seem, therefore, at odd with experiments.

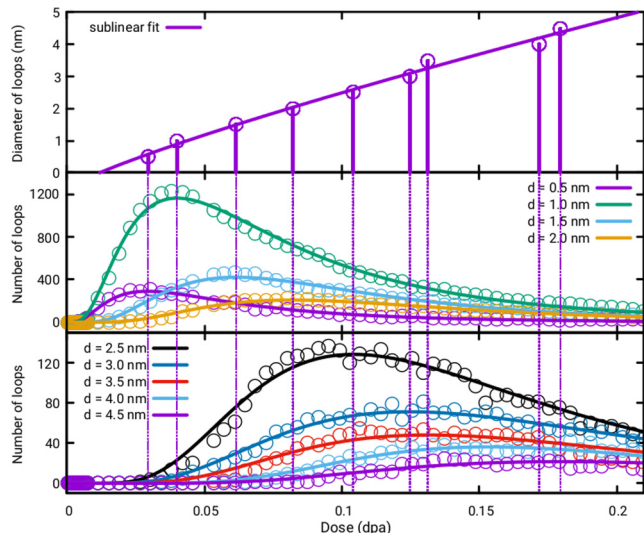


FIG. 10. Growth of loops observed in the simulations performed with the Akamatsu potentials.⁴⁶ Bottom panels: evolution of the number of loops of different diameters (d in nm) as a function of doses (open circles) and fit with lognormal laws (lines). Upper panel: diameters of loops—taken as the global maximum of the lognormal laws for each diameter of both bottom panels—as a function of dose (open circles) and fit with a sublinear law. Vertical lines (full and dashed purple lines) are the global maximum of the lognormal fits for each diameter of loops.

Three qualitative statements can be put forward to explain this discrepancy. First, one may question the reliability of the empirical potentials used. However, this is unlikely since both potentials show similar trends despite having been designed for quite different purposes, and particularly because they reproduce quite well numerous complex properties—including stacking fault energies (see Table I) and core energy of screw dislocation in the case of Henkelman potentials.⁵⁴ Second, the high rate of defects created by the FPA—though handled by the Berendsen barostat—could be

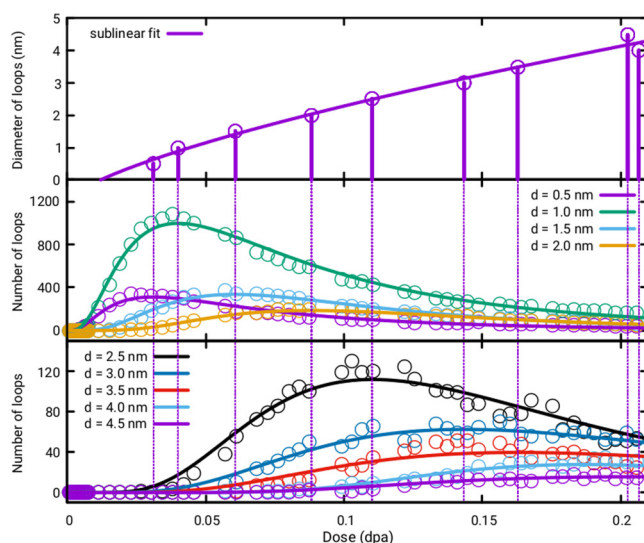


FIG. 11. Growth of loops observed in the simulations performed with the Henkelman potentials.⁴⁷ Symbols and lines are the same as in Fig. 10.

TABLE I. Stacking fault energies (γ_{SF}), inverse of area density of MgO interstitials (α), and coefficients of Eq. (1) for the three {001}, {011}, and {111} planes for both Henkelman and Akamatsu potentials.

| Planes | Akamatsu | | | Henkelman | | |
|--|-----------|-----------|-----------|-------------------|-------------------|-----------|
| | {001} | {011} | {111} | {001} | {011} | {111} |
| γ_{SF} (eV/Å ²) DM | 0.1105 | 0.0506 | 0.1392 | 0.1386 | 0.0599 | 0.1526 |
| γ_{SF} (J/m ²) DM | 1.77 | 0.81 | 2.23 | 2.22 ^a | 0.96 ^a | 2.45 |
| γ_{SF} (J/m ²) DFT ^b | 2.18 | 1.05 | 2.47 | 2.18 | 1.05 | 2.47 |
| α (Å ²) | 54.545 6 | 78.714 1 | 59.820 9 | 54.545 6 | 78.714 1 | 59.820 9 |
| $\alpha\gamma_{SF}/4\pi$ (eV) | 0.479 636 | 0.316 952 | 0.662 647 | 0.601 607 | 0.375 206 | 0.726 436 |
| a_1 | -90.331 7 | -71.238 3 | -103.58 | -114.631 | -41.058 1 | -102.947 |
| a_2 | +44.705 1 | +34.131 | +53.376 6 | +55.564 7 | +27.371 5 | +55.333 1 |
| a_3 | -4.075 89 | -1.679 11 | -6.116 62 | -5.945 85 | -0.852 054 | -6.467 56 |

^aDFT values from Ref. 54.^bDFT values from Ref. 68.

challenged as well. Thus, even if simulations are done at constant pressure, local residual stresses are present in the supercells during the FPA process. These local residual stresses, which come from the high rate of Frenkel pair introduction, impose high densities of loops and point defects within short relaxation times. Stresses are known⁶⁹ to strongly modify the relative stability of the stacking fault energies. It might homogenize the amount of loops in the three lying planes. Third, while simulations are performed using periodic boundary conditions, defects are created only in a thin near-surface layer in the experiments, being ion or electron irradiation. As a result, the layer where the defect-induced stresses arise lies on an undamaged substrate, which leads to a non-uniform stress distribution; stresses in the plane of the sample are greater because the expansion of the material in the surface plane is blocked, but expansion in the direction perpendicular to the surface is possible. This anisotropic stress distribution may affect the geometry of the dislocations formed in the subsurface layer.

However, a quantitative explanation can be provided by the evaluation of the relative stability of the $\frac{1}{2}\langle 110 \rangle$ interstitial dislocation loops in the three different planes as a function of their size. To explore this path, we use the Babel code developed by Clouet⁷⁰ to generate different loops in 4 096 000-atoms supercells—or $33 \times 33 \times 33 \text{ nm}^3$. We build circular $\frac{1}{2}\langle 110 \rangle\{001\}$, $\frac{1}{2}\langle 110 \rangle\{110\}$, and $\frac{1}{2}\langle 110 \rangle\{111\}$ loops of increasing sizes, i.e., increasing radius R , and, subsequently, relax them by static energy minimization at constant volume. Their formation energies are then calculated by energy difference with a perfect cell containing the same number of atoms. The results are fitted to the equation established by Alexander *et al.*⁷¹ The asymptotic value at large radii R is known⁷² to be proportional to the stacking fault energy following the relation $\pi R^2 \gamma_{SF}$. Rewriting with $\pi R^2 = \alpha/4\pi \times n$ (n being the number of interstitials in the loop, while α being related to the surface density of atoms in the loop), the formation energy of a loop reads

$$E_f(n) = \frac{\alpha}{4\pi} \gamma_{SF} + \frac{a_1}{n} + \frac{a_2}{\sqrt{n}} + \frac{a_3 \ln(n)}{\sqrt{n}}, \quad (1)$$

in which a_1 , a_2 , and a_3 constants are the fitting parameters. The

results of the fit to Eq. (1) are shown in Fig. 12, and the parameters are listed in Table I for $\frac{1}{2}\langle 110 \rangle$ loops lying in {111}, {110}, and {001} planes with the Akamatsu and Henkelman potentials.

As expected, the formation energies (per MgO formula unit) of the loops for the three planes decrease with loop size for both potentials. The formation energies are quite similar regardless of the specific habit planes up to around few hundreds of MgO anti-Schottky (see Fig. 12). The loops in {110} planes exhibit slightly higher values, but this remains marginal (less than 0.1 eV/MgO) compared to the absolute values of formation energies (of the order of 1 eV/MgO). Indeed, at large diameters, it is more favorable for a

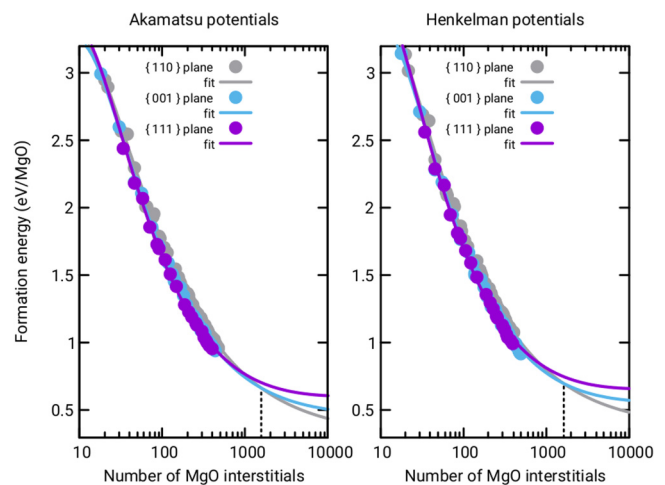


FIG. 12. Formation energies (eV/MgO) of circular prismatic $\frac{1}{2}\langle 110 \rangle$ loops lying in the {110} plane (gray), {001} plane (blue), and {111} plane (purple) as a function of interstitials in the loops calculated by static energy minimization. Both Akamatsu and Henkelman data were fitted using Eq. (1) with values reported in Table I. Crossing points between {110} and {001} planes are indicated by vertical dashed lines and are, respectively, 1536 and 1610 MgO interstitials for Akamatsu and Henkelman.

$\frac{1}{2}\langle 110 \rangle$ loop to be in a $\{110\}$ plane compared to the two other planes. The crossing points are at 1536 and 1610 MgO interstitials, respectively, for Akamatsu and Henkelman potentials, which corresponds to diameters of $\frac{1}{2}\langle 110 \rangle\{110\}$ loops of around 14.2 and 15.7 nm. Therefore, below the critical diameters of roughly 15 nm, $\frac{1}{2}\langle 110 \rangle$ loops can lie indifferently in all the three planes. And above these critical diameters, $\frac{1}{2}\langle 110 \rangle\{110\}$ loops only are stable at the expense of the other loops. This trend nicely correlates with experimental observations.^{24,36,37,39,40}

Such a critical diameter of roughly 15 nm is never reached in our simulations: loops hardly attain diameters of 10 nm (see Figs. 2 and 3). This upper bound can be easily understood based on geometrical considerations. Having in mind that the supercell size is a cube of 40 nm edges, it is straightforward that any loop having a diameter of more than 15 nm would strongly interact with itself because of periodic boundary conditions. As a consequence, it would readily anneal or reorganize into dislocation forest. And that is precisely what is evidenced from FPA calculations (see again Figs. 2 and 3). On the contrary, loops with diameters smaller than 10 nm may stabilize in the supercell. Their lying planes are indifferent according to the small formation energy differences they exhibit, and this explains the results presented above.

However, we observe at the end of the simulations (at around 1 dpa) that the dislocations network—not the loops themselves—defines domains separated along $\{110\}$ planes. This provides a clue that big enough supercells could allow the stabilization of $\frac{1}{2}\langle 110 \rangle\{100\}$ loops at the expense of the other planes.

IV. CONCLUSION

Using two empirical potentials—Akamatsu⁴⁵ and Henkelman⁴⁸—we investigate, in the present work, the response of MgO periclase to damages induced by irradiation. We use the Frenkel pairs accumulation methodology^{42,43,51} in order to observe the evolution of the microstructure with dose. Doing so, we mimic damages produced by electron irradiation rather than any other types of irradiations, in the recombination regime at low temperatures⁵¹ where diffusion is hindered. Indeed, the combined effect of the dose rate and temperature cannot be investigated in the present work and is, therefore, outside the scope of our conclusions.

With these simulations, we can link the evolution of defects (vacancies, interstitials, cavities) and dislocations as a function of the irradiation dose with both lattice swelling—which is related to the change of lattice parameter—and volume swelling—that is a measure of the modification of the total volume. This link is possible because most experimental observations are reproduced—at least qualitatively—by the simulations done with the two empirical potentials used, supporting the robustness and the generic character of the results in the low temperature regime.

One of the main results of our simulations concerns volume and lattice swellings. We observe the same divergence between lattice and volume swellings at around 0.2 dpa as seen experimentally. Below 0.2 dpa, lattice swelling perfectly matches the volume swelling following a trend^{1,35,39–41,45} observed in Urania, for example:⁵¹ isolated vacancies and interstitials as well as $\frac{1}{2}\langle 110 \rangle$ loops contribute in order of appearance to both swellings. Above 0.2 dpa, the behavior of lattice and volume swellings diverges.

Lattice swelling gently moderates, mainly because loops recombine into forest dislocations with a strong decrease in dislocation density. This is again in line with expectations. On the contrary, volume swelling increases sharply under the action of vacancies.⁶¹ Interestingly, the acceleration of the volume swelling is related to the occurrence of relatively big voids, made of up to $(\text{MgO})_{16}$ Schottky defects.

The nucleation and growth of $\frac{1}{2}\langle 110 \rangle$ loops is also carefully analyzed in the present work. Similar nucleation mechanisms as reported previously^{29–32} are observed, which demonstrate that FPA captures timescales that are far higher than expected. Interstitials of magnesium and oxygen progressively gather together. They adopt 3D or 2D shapes below $(\text{MgO})_4$ anti-Schottky, before their stabilization as platelets. These platelets can be defined as loops when interstitial clusters are of more than $(\text{MgO})_6$ anti-Schottky. These loops further grow seizing interstitials around. Their growth follows a sublinear law with exponents (for both Akamatsu and Henkelman potentials) close to experimental estimations at low temperatures.^{19–21} However, their lying planes are not limited to the $\{110\}$ plane as systematically seen in the experiments.^{19,34,36} A significant part of loops lie in the $\{001\}$ and $\{111\}$ planes. This is likely related to the very similar relative stabilities of small loops in all the three $\{001\}$, $\{110\}$, and $\{111\}$ planes for $\frac{1}{2}\langle 110 \rangle$ loops in simulations. However, loops with the diameter of more than 15 nm show lower formation energies than the two others, making very probable their preferential stabilization in very huge super-cells.

One has to mention that apart from the inherent limited ability of empirical potentials to describe properly dislocations, foreign ingredients for simulations such as residual stresses, proximity of surfaces, and long range diffusion can also explain the discrepancy with experiments for small loops. As a final remark, no elongated loop is observed in our simulations—being FPA or static calculations. This might be related to their size—seen as micrometers^{19,20}—or to any other foreign ingredient mentioned above.

ACKNOWLEDGMENTS

This work was granted access to the HPC resources of the TGCC computing center, under the DARI Allocation No. A0120913433.

AUTHOR DECLARATIONS

Conflict of Interest

The authors have no conflicts to disclose.

Author Contributions

Alain Chartier: Conceptualization (equal); Data curation (equal); Formal analysis (equal); Funding acquisition (lead); Investigation (equal); Resources (equal); Software (equal); Validation (equal); Visualization (equal); Writing – original draft (lead); Writing – review & editing (lead). **Paul Fossati:** Data curation (equal); Formal analysis (equal); Investigation (equal); Software (equal); Validation (equal); Visualization (equal); Writing – review & editing (equal). **Laurent Van Brutzel:** Validation (equal); Writing – review & editing (equal). **Orest Dorosh:** Data curation (equal); Formal analysis (equal); Investigation (equal); Software (equal); Validation

(equal); Writing – review & editing (equal). **Jacek Jagielski:** Funding acquisition (equal); Resources (equal); Validation (equal); Writing – review & editing (equal).

DATA AVAILABILITY

The data that support the findings of this study are available from the corresponding author upon reasonable request.

REFERENCES

- ¹S. J. Zinkle, in *Comprehensive Nuclear Materials*, 2nd ed., edited by R. J. M. Konings (Elsevier, 2020), Chap. 1.04, p. 91.
- ²J. Jagielski and L. Thomé, *Nucl. Instrum. Methods Phys. Res. Sect. B* **266**, 1212 (2008).
- ³J. Jagielski and L. Thomé, *Appl. Phys. A* **97**, 147 (2009).
- ⁴W. J. Weber, R. C. Ewing, C. R. A. Catlow, T. Diaz de la Rubia, L. W. Hobbs, C. Kinoshita, H. Matzke, A. T. Motta, M. Nastasi, E. K. H. Salje, E. R. Vance, and S. J. Zinkle, *J. Mater. Res.* **13**, 1434 (1998).
- ⁵A. J. Tench and M. J. Duck, *J. Phys. C: Solid State Phys.* **6**, 1134 (1973).
- ⁶D. Caceres, I. Vergara, R. Gonzales, and Y. Chen, *Phys. Rev. B* **66**, 024111 (2002).
- ⁷M. Cao, Y. Ma, X. Wang, C. Ma, W. Zhou, X. Wang, W. Tan, and J. Du, *AIP Adv.* **7**, 056413 (2017).
- ⁸Y. Chen, D. L. Trueblood, O. E. Schow, and H. T. Tohver, *J. Phys. C: Solid State Phys.* **3**, 2501 (1970).
- ⁹L. E. Halliburton and L. A. Kappers, *Solid State Commun.* **26**, 111 (1978).
- ¹⁰G. J. Russel, E. A. Ammar, and J. S. Thorp, *J. Mater. Sci.* **11**, 1961 (1976).
- ¹¹D. G. Martin, *J. Phys. C: Solid State Phys.* **1**, 333 (1968).
- ¹²A. van Veen, M. A. van Huis, A. V. Fedorov, H. Schut, F. Labohm, B. J. Kooij, and J. T. M. De Hosson, *Nucl. Instrum. Methods Phys. Res. Sect. B* **191**, 610 (2002).
- ¹³S. J. Zinkle, *Nucl. Instrum. Methods Phys. Res. Sect. B* **286**, 4 (2012).
- ¹⁴H. R. Zhang, R. Egerton, and M. Malac, *Nucl. Instrum. Methods Phys. Res. Sect. B* **316**, 137 (2013).
- ¹⁵J. Mulroue, B. P. Uberuaga, and D. M. Duffy, *J. Phys.: Condens. Matter* **25**, 065502 (2013).
- ¹⁶C. Scholz and P. Ehrhart, *MRS Proc.* **279**, 427 (1992).
- ¹⁷A. E. Hughes, *J. Phys. Colloq.* **34**, C9-515–C9-518 (1973).
- ¹⁸A. Debelle, J.-P. Crocombette, A. Boulle, E. Martinez, B. P. Uberuaga, D. Bachiller-Perea, Y. Hadad, F. Garrido, L. Thomé, and M. Béhar, *Phys. Rev. Mater.* **2**, 083605 (2018).
- ¹⁹A. I. Van Sambeek, R. S. Averback, C. P. Flynn, M. H. Yang, and W. Jäger, *J. Appl. Phys.* **83**, 7576 (1998).
- ²⁰B. P. Uberuaga, E. Martinez, D. Perez, and A. F. Voter, *Comput. Mater. Sci.* **147**, 282 (2018).
- ²¹B. Henderson and D. H. Bowen, *J. Phys. C: Solid State Phys.* **4**, 1487 (1971).
- ²²C. Kinoshita, K. Hayashi, and S. Kitajima, *Nucl. Instrum. Methods Phys. Res. Sect. B* **1**, 209 (1984).
- ²³R. A. Youngman, L. W. Hobbs, and T. E. Mitchell, *J. Phys. Colloq.* **41**, C6-227–C6-231 (1980).
- ²⁴T. Sonoda, H. Abe, C. Kinoshita, and H. Naramoto, *Nucl. Instrum. Methods Phys. Res. Sect. B* **127–128**, 176 (1997).
- ²⁵E. Wendler, K. Gärtner, and W. Wesch, *Nucl. Instrum. Methods Phys. Res. Sect. B* **257**, 488 (2007).
- ²⁶E. Wendler, K. Gärtner, and W. Wesch, *Nucl. Instrum. Methods Phys. Res. Sect. B* **266**, 2872 (2008).
- ²⁷B. Park, W. J. Weber, and L. R. Corrales, *Nucl. Instrum. Methods Phys. Res. Sect. B* **166–167**, 357 (2000).
- ²⁸B. A. Petersen, B. Liu, W. J. Weber, and Y. Zhang, *J. Nucl. Mater.* **486**, 122 (2017).
- ²⁹L. Kittiratanawasin, R. Smith, B. P. Uberuaga, and K. Sickafus, *Nucl. Instrum. Methods Phys. Res. Sect. B* **268**, 2901 (2010).
- ³⁰B. P. Uberuaga, R. Smith, A. R. Cleave, G. Henkelman, R. W. Grimes, A. F. Voter, and K. E. Sickafus, *Phys. Rev. B* **71**, 104102 (2005).
- ³¹B. J. Cowen and M. S. El-Genk, *J. Mater. Sci. Eng.* **10**, 7 (2021), <https://www.hilarispublisher.com/open-access/irradiation-effect-predictions-in-mgo-using-molecular-dynamics-simulations-of-incident-single-and-multiple-au-ions-73726.html>.
- ³²D. S. Aidhy, P. C. Millet, D. Wolf, S. R. Phillpot, and H. Huang, *Scr. Mater.* **60**, 691 (2009).
- ³³B. P. Uberuaga, R. Smith, A. R. Cleave, G. Henkelman, R. W. Grimes, A. F. Voter, and K. E. Sickafus, *Nucl. Instrum. Methods Phys. Res. Sect. B* **228**, 260 (2005).
- ³⁴B. P. Uberuaga, A. F. Voter, K. E. Sickafus, A. Cleave, R. W. Grimes, and R. Smith, *J. Comput. Aided Mater. Des.* **14**, 183 (2007).
- ³⁵B. P. Uberuaga, R. Smith, A. R. Cleave, F. Montalenti, G. Henkelman, R. W. Grimes, A. F. Voter, and K. E. Sickafus, *Phys. Rev. Lett.* **92**, 115505 (2004).
- ³⁶L. L. Horton, J. Bentley, and M. B. Lewis, *Nucl. Instrum. Methods Phys. Res. Sect. B* **16**, 221 (1986).
- ³⁷Y. Satoh, C. Kinoshita, and K. Nakai, *J. Nucl. Mater.* **179–181**, 399 (1991).
- ³⁸D. Bachiller-Perea, A. Debelle, L. Thomé, and M. Behar, *J. Nucl. Mater.* **478**, 268 (2016).
- ³⁹R. S. Wilks, *J. Nucl. Mater.* **26**, 137 (1968).
- ⁴⁰G. W. Groves and A. Kelly, *Philos. Mag.* **8**, 1437 (1963).
- ⁴¹J. Narayan and J. Washburn, *J. Appl. Phys.* **43**, 4862 (1972).
- ⁴²C. Kinoshita, T. Sonoda, and A. Manabe, *Philos. Mag. A* **78**, 657 (1998).
- ⁴³F. W. Clinard, G. F. Hurley, and L. W. Hobbs, *J. Nucl. Mater.* **108–109**, 655 (1982).
- ⁴⁴R. W. Davidge, *J. Nucl. Mater.* **25**, 75 (1968).
- ⁴⁵D. Bachiller-Perea, A. Debelle, L. Thomé, and J.-P. Crocombette, *J. Mater. Sci.* **51**, 1456 (2016).
- ⁴⁶T. Akamatsu and K. Kawamura, *Mol. Simul.* **21**, 387 (1999).
- ⁴⁷G. Henkelman, B. P. Uberuaga, D. J. Harris, J. H. Harding, and N. L. Allan, *Phys. Rev. B* **72**, 115437 (2005).
- ⁴⁸J.-P. Crocombette, A. Chartier, and W. J. Weber, *Appl. Phys. Lett.* **88**, 051912 (2006).
- ⁴⁹A. Chartier, G. Catillon, and J.-P. Crocombette, *Phys. Rev. Lett.* **102**, 155503 (2009).
- ⁵⁰A. P. Thompson, H. M. Aktulga, R. Berger, D. S. Bolintineanu, W. M. Brown, P. S. Crozier, P. J. in 't Veld, A. Kohlmeyer, S. G. Moore, T. D. Nguyen, R. Shan, M. J. Stevens, J. Tranchida, C. Trott, and S. J. Plimpton, *Comput. Phys. Commun.* **271**, 108171 (2022).
- ⁵¹Y. Ito and M. Toriumi, *J. Geophys. Res.* **112**, B04206, <https://doi.org/10.1029/2005JB003685> (2007).
- ⁵²M. Landeiro Dos Reis, P. Carrez, and P. Cordier, *Phys. Rev. Mater.* **5**, 063602 (2021).
- ⁵³J. Amodeo, E. Maras, and D. Rodney, *npj Comput. Mater.* **7**, 1 (2021).
- ⁵⁴P. Carrez, J. Godet, and P. Cordier, *Comput. Mater. Sci.* **103**, 250 (2015).
- ⁵⁵A. Chartier, C. Onofri, L. Van Brutzel, C. Sabathier, O. Dorosh, and J. Jagielski, *Appl. Phys. Lett.* **109**, 181902 (2016).
- ⁵⁶H. Balboa, L. Van Brutzel, A. Chartier, and Y. Le Bouar, *J. Nucl. Mater.* **512**, 440 (2018).
- ⁵⁷L. V. Brutzel, P. Fossati, and A. Chartier, *J. Nucl. Mater.* **567**, 153834 (2022).
- ⁵⁸C. Meis and A. Chartier, *J. Nucl. Mater.* **341**, 25 (2005).
- ⁵⁹M. Jiang, H. Gong, B. Zhou, H. Xiao, H. Zhang, Z. Liu, and X. Zu, *J. Nucl. Mater.* **540**, 152379 (2020).
- ⁶⁰E. Moore, C. Guéneau, and J.-P. Crocombette, *J. Solid State Chem.* **203**, 145 (2013).
- ⁶¹E. A. Kotomin and A. I. Popov, *Nucl. Instrum. Methods Phys. Res. Sect. B* **141**, 1 (1998).
- ⁶²K. Nordlund, S. J. Zinkle, A. E. Sand, F. Granberg, R. S. Averback, R. Stoller, T. Suzudo, L. Malerba, F. Banhart, W. J. Weber, F. Willaime, S. L. Dudarev, and D. Simeone, *Nat. Commun.* **9**, 1 (2018).
- ⁶³A. Stukowski and K. Albe, *Modell. Simul. Mater. Sci. Eng.* **18**, 085001 (2010).
- ⁶⁴See <https://github.com/wojdyr/debyer> for information about the Debyer software.

- ⁶⁵T. Jourdan and M. Nastar, *J. Appl. Phys.* **131**, 225103 (2022).
- ⁶⁶A. Chartier; and M. C. Marinica, *Acta Mater.* **180**, 141 (2019).
- ⁶⁷R. B. Bergmann and A. Bill, *J. Cryst. Growth* **310**, 3135 (2008).
- ⁶⁸J. Amodeo, P. Carrez, and P. Cordier, *Philos. Mag.* **92**, 1523 (2012).
- ⁶⁹P. Carrez, D. Ferré, and P. Cordier, *IOP Conf. Ser.: Mater. Sci. Eng.* **3**, 012011 (2009).
- ⁷⁰E. Clouet, see <http://emmanuel.clouet.free.fr/Programs/Babel> for Babel software.
- ⁷¹R. Alexander, M.-C. Marinica, L. Proville, F. Willaime, K. Arakawa, M. R. Gilbert, and S. L. Dudarev, *Phys. Rev. B* **94**, 024103 (2016).
- ⁷²G. W. Wolfer, "Fundamental properties of defects in metals," in *Comprehensive Nuclear Materials* (Elsevier Amsterdam, The Netherlands, 2020), pp. 1–49.